9-12-2014

Radiation Damage in Permanent Magnet Lenses

Christopher Danly

Christopher R. Danly
Candidate

Nuclear Engineering
Department

This thesis is approved, and it is acceptable in quality and form for publication:

Approved by the Thesis Committee:

Gary W. Cooper , Chairperson

Anil K. Prinja

Frank E. Merrill

Salvador B. Rodriguez

Radiation Damage in Permanent Magnet Lenses

by

Christopher Danly

B.S., Physics, Lehigh University, 2010

THESIS

Submitted in Partial Fulfillment of the

Requirements for the Degree of

Master of Science

Nuclear Engineering

The University of New Mexico

Albuquerque, New Mexico

July, 2014

Acknowledgments

I would like to thank the following people: My LANL mentor, Frank Merrill, for his guidance; David Barlow, whose magnet lab and expertise I used to make the measurements presented here; the LANL pRad team for their support with these measurements. I would also like to express my gratitude to my professors for their patience and flexibility.

Radiation Damage in Permanent Magnet Lenses

by

Christopher Danly

B.S., Physics, Lehigh University, 2010

M.S., Nuclear Engineering, University of New Mexico, 2014

Abstract

Proton radiography techniques in use at Los Alamos National Lab and elsewhere depend upon permanent magnet quadrupoles in their magnetic optics. Radiation exposure during radiography experiments is known to damage these lenses and degrade image quality. This effect is studied under controlled conditions, leading to the conclusion that nonuniform radiation damage is inherent to the quadrupole configuration and results in increased multipole moments which degrade the imaging performance. Studies on magnet samples suggest that Samarium Cobalt is at least a thousand times more radiation-tolerant and should be used as a replacement for NdFeB in magnetic lenses for high-dose proton radiography.

Contents

List of Figures **ix**

List of Tables **xii**

1 Introduction **1**

1.1 Overview 1

1.2 Proton Radiography Background 2

1.3 LANL pRad 3

1.4 Literature Review 8

2 First Experiment **10**

2.1 Overview 10

2.2 Samples and Instrumentation 14

2.2.1 Magnet 14

2.2.2 Radiation 14

2.2.3 Instrumentation 15

2.3 Experimental considerations 16

2.4 Data 17

2.5 Analysis 17

2.5.1 Dose estimation 18

2.5.2 Magnetic field data 21

2.5.3 Synthesis 22

2.6 Results 23

3 Second Experiment **26**

3.1 Overview 26

3.2 Samples and Instrumentation 27

3.2.1 Radiation 27

3.2.2 Magnet characteristics 27

3.2.3 Instrumentation 28

3.3 Data 29

3.4 Analysis 29

3.4.1 Dose analysis 29

3.4.2 Beam profile 31

3.4.3 Droop 32

3.4.4 Error Analysis 33

3.5 Results 35

4 Conclusions **38**

5 Continuing and Future Work **39**

Appendices **41**

A PMQ experiment **42**

A.1 Data 45

A.2 Listing of MCNP deck 47

B Material sample experiment **54**

B.1 Data 54

References **56**

List of Figures

1.1 Sample proton radiograph of an explosively shocked sample [2]. . . . 2

1.2 LANL pRad 3X Magnifier. 4

1.3 Slice of 3X magnifier showing segment numbering. [10] 5

1.4 Image quality degradation due to demagnetization over the course of a tomography run on a meteorite [11]. Images are the same view of the object; note blurring and substantial loss of fine details in right image. 5

1.5 Map of 3X magnifier after extended use. Colors represent different longitudinal segments ("slices"). [10] 6

1.6 Measurement of 7X magnifier after use. Colored lines represent different lenses; dashed lines are the values after remagnetization. [12] . 7

2.1 Configuration of magnet and target for experiment. 12

2.2 Experimental setup. 13

2.3 PMQ used for experiment, with cover removed and probe holder installed 15

2.4 Magnetic field at each segment tip as a function of protons delivered. Vertical scale in Gauss, horizontal scale in 10^{13} protons. 17

2.5 Flattened radiograph from image plate placed downstream of the magnet. X and Y scale in pixels, Color scale arbitrary. 18

2.6 MCNPX geometry plotted in magnet plane (top) and vertical plane (bottom). 19

2.7 Energy deposition in magnet from MCNPX. X and Y scales in cm, color scale in kGy. 20

2.8 Zero-dose initial measurement compared to sinusoidal expected form. Vertical scale in cm, horizontal scale in radians. 21

2.9 H_{mod} from Opera. X and Y scales in cm, color scale in Oersted. . . . 22

2.10 Damage as a function of dose, averaged over like segments. 23

2.11 Higher-order multipole moments increased by radiation damage . . . 24

2.12 Product of H_{mod} and Dose. X, Y scales in cm, color scale in arb. units. 25

2.13 Plot of final field strength as a function of angle. Radial scale in kGauss. 25

3.1 Magnet samples. Top: First batch, NdFeB in thicknesses of 16, 8, 4, and 2 mm. Bottom: NdFeB and SmCo in 3 and 2 mm each. 28

3.2 Magnet sample in paper and foam mount. 29

3.3 Raw phosphor image of NAC sample. Scale in pixels. 30

3.4 Image dewarped, mapped to real-world coordinates, and divided by beam profile. X and Y scales in cm, color scale is intensity ratio. . . 31

3.5 Gaussian fit to dewarped phosphor image. Scale is 0.1 mm pixels. . 32

3.6 Gaussian with magnet location for integration. X and Y scales in cm. 33

3.7 Demagnetization as a function of proton count for all NdFeB samples. 34

3.8 Demagnetization as a function of dose for selected samples 35

3.9 D20, dose to demagnetize by 20% as a function of permanence coefficient. Compared for present data, Ito *et al.* [6] and Talvitie *et al.* [17] 36

3.10 D20 normalized to 2mm sample for various samples. 37

A.1 Additional photos showing experimental setup. 43

A.2 Probe inserted into PMQ 44

List of Tables

A.1 **B field in PMQ (Gauss) as a function of dose** 45

A.2 **Individual segments measured after damage and after re-magnetization. Units of Gauss.** 46

B.1 **First batch of samples. Magnetic moment in uV*sm** 54

B.2 **Second batch of samples. Magnetic moment in uV*sm** . . . 54

B.3 **Third batch of samples. Magnetic moment in uV*sm** 55

B.4 **Cumulative dose at various measurements (Gy)** 55

Chapter 1

Introduction

1.1 Overview

Accelerator-driven proton radiography is a technique which was developed at Los Alamos National Laboratory (LANL) in the 1990s to allow high-speed transmission imaging of dynamic experiments[1]. An accelerator provides high-energy protons, magnetic lenses are used to focus the protons between an object and an image plane, a collimator provides contrast, and a detection system records the image.

This technique is now in use around the world – notably, in the US, Russia, China, and Germany. The proton radiography (pRad) facility at LANL uses permanent-magnet quadrupoles for magnifying lenses[3, 4], and a system recently commissioned at GSI-Darmsdadt[5] uses permanent magnets for its primary lenses (a 5X magnifier).

Irradiation of permanent magnets by high energy protons or by neutrons, such as those produced when the beam interacts with the collimator, is known to cause demagnetization [6, 7, 8]. However, in radiography experiments at LANL the image quality has been observed to degrade faster than would be expected due to decreased

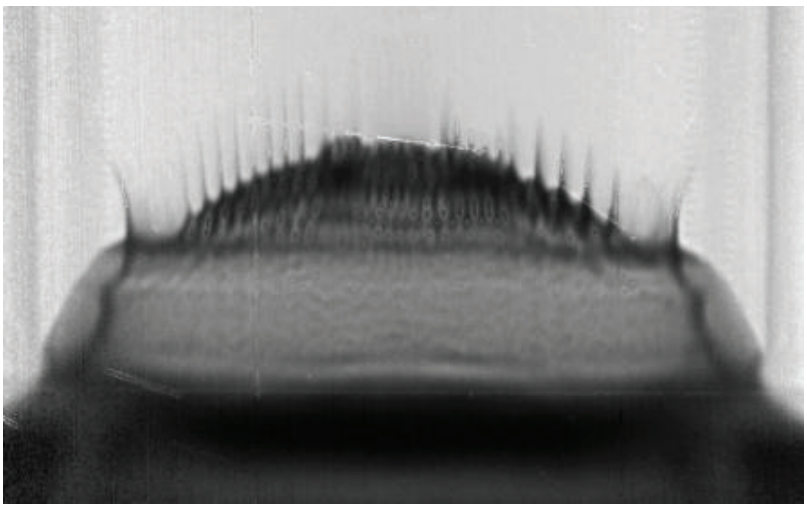

Figure 1.1: Sample proton radiograph of an explosively shocked sample [2].

magnetic lens strength alone. This thesis reports work performed to study and understand this phenomenon.

1.2 Proton Radiography Background

Modern proton radiography relies on a proton source (accelerator), magnetic optics to create images, and a collimator to produce contrast. The system designed at LANL uses two quadrupole doublets to produce a point-to-point focus between the object location and the image plane.

An ideal quadrupole lens has a magnetic field whose intensity varies linearly with radius (zero at the center of the magnet) and whose direction is focusing in one axis and defocusing in the other. Two quadrupoles rotated 90° relative to each other are paired to produce a quadrupole doublet, which first focuses and then defocuses in X and the opposite in Y.

The system is focused for a particular energy, and the optics produce a Fourier plane in between the two lens pairs. Particles (from any point in the object plane) with the design energy pass through the center of the fourier plane; particles which have Coulomb scattered in the object traverse the plane at a radius proportional to the amount of scattering. A collimator is placed around the fourier plane to selectively block protons which have a positional deviation above a certain threshold; this produces contrast for imaging thin samples. The proton interaction in the collimator also produces spallation neutrons, which then impinge on the magnetic lenses, particularly the third lens which is directly downstream. This, along with irradiation by the proton beam during tuning, has been observed to cause damage to the magnets.

1.3 LANL pRad

The pRad facility at LANL is used to conduct a wide variety of experiments of interest to defense programs, materials science, medical imaging, and other areas. Experiments cover a wide range of time and length scales. Dynamic experiments - driven by explosives, pulsed power systems, or powder guns - use high-speed framing cameras to record several dozen images at sub-microsecond frame spacing. An example of a dynamic experiment studying Richtmyer-Meshkov instability[2] is shown in Figure 1.1. Metallurgy experiments can involve movies of quasistatic systems at few-Hertz rates, and static experiments are also conducted. Tomography of static objects can be accomplished by taking images rapidly as the object is rotated.

Three magnetic lenses are used for proton radiography at LANL and are selected depending on the resolution and field of view required for the experiment. The identity lens (1X magnification) uses electromagnets; 3X and 7X magnifier lenses are composed of multiple permanent magnet quadrupoles (PMQs). Each PMQ is made up of many individual magnets which are arranged radially in a Halbach configuration[9]

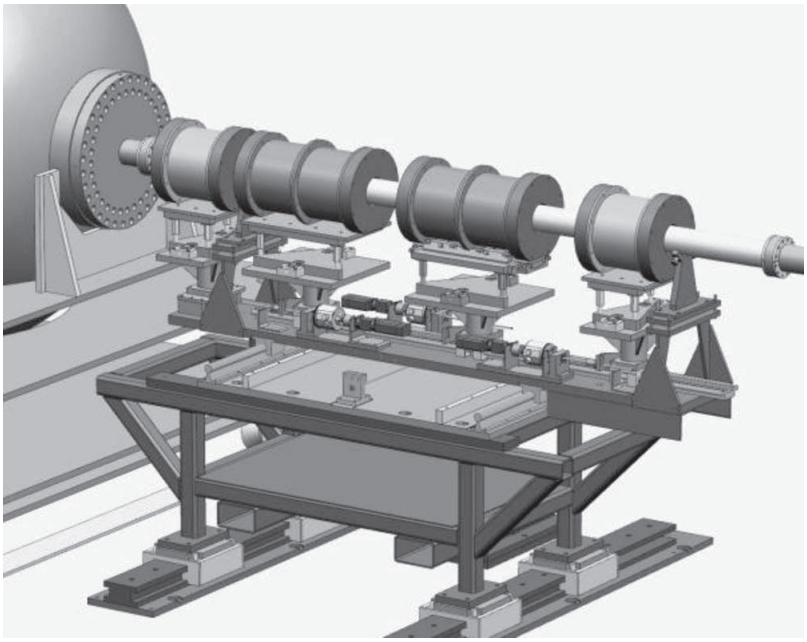

Figure 1.2: LANL pRad 3X Magnifier.

and also stacked to provide the required field strength and length. The pRad 3X magnifier is shown in Figure 1.2 and details may be found in Merrill *et al.* [3]. The 7X magnifier is discussed in Mottershead *et al.* [4]. The layout of a 3X magnifier PMQ is shown in Figure 1.3.

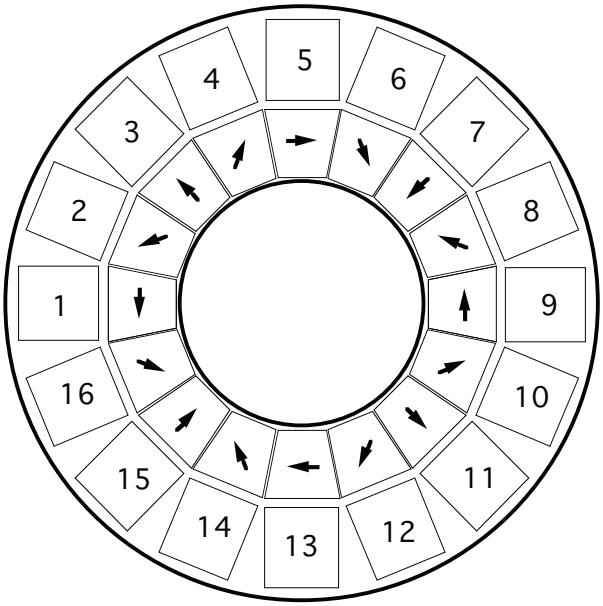

Figure 1.3: Slice of 3X magnifier showing segment numbering. [10]

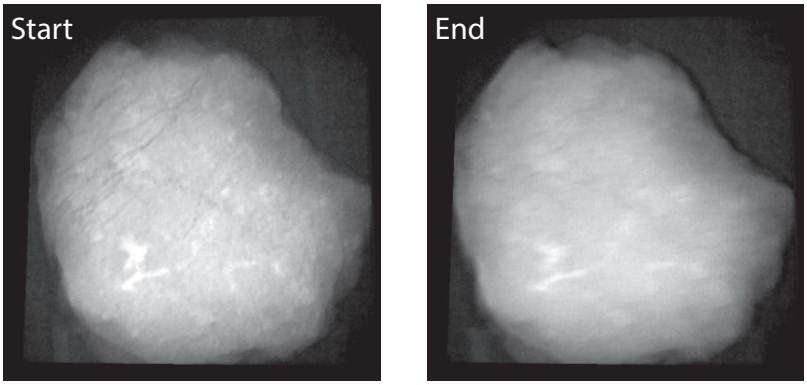

Figure 1.4: Image quality degradation due to demagnetization over the course of a tomography run on a meteorite [11]. Images are the same view of the object; note blurring and substantial loss of fine details in right image.

The press towards better resolution has led to increased use of the 3X and 7X magnifier lenses. Typical static or dynamic experiments involve taking tens to low hundreds of images; tomography experiments may require thousands. As the magnifier lenses are used, radiation exposure damages the permanent magnets and produces, over time, a noticeable degradation in the quality of the images. The damage is worse with the 7X magnifier, which has a smaller aperture. A set of images from the beginning and end of a high-dose tomography run with the 7X magnifier are shown in Figure 1.4.

When the magnifier lenses become unusable, or at the end of the accelerator run cycle, they are removed from service and their fields mapped. The poles consistently show the least damage; the tangential segments (1, 5, 9, and 13 in the numbering scheme used here) consistenly show the most. A set of measurements of the 3X and 7X magnifier are shown in Figures 1.5 and 1.6.

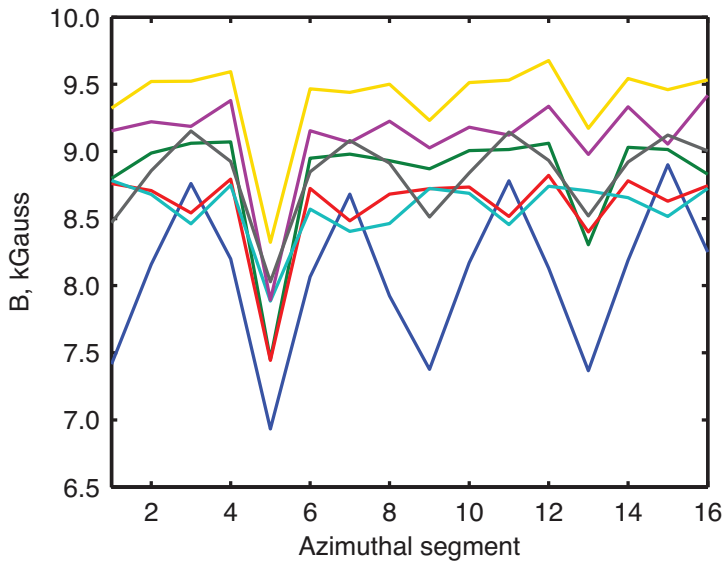

Figure 1.5: Map of 3X magnifier after extended use. Colors represent different longitudinal segments ("slices"). [10]

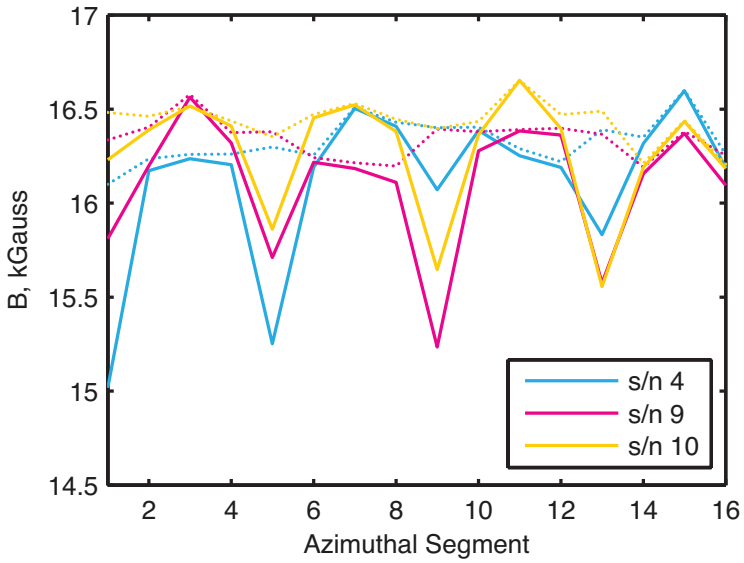

Figure 1.6: Measurement of 7X magnifier after use. Colored lines represent different lenses; dashed lines are the values after remagnetization. [12]

After mapping, the magnet segments are remagnetized and the PMQs reassembled; the initial quality of the PMQ is restored. However, this process is expensive and time-consuming, so a better solution is desired.

1.4 Literature Review

A substantial body of literature exists on the effects of radiation on permanent magnet materials.

Blackmore [13] discussed in 1985 the application of rare-earth permanent magnet quadrupoles in accelerator beam optics. He reported on the demagnetization of single samples of samarium-cobalt when irradiated with 500 MeV protons at doses up to 10^8 Gray; dose was measured with activation foils. A sample of NdFeB was also irradiated but showed demagnetization at such a low dose that it was dismissed for the application discussed. Blackmore stated that the SmCo PMQs at TRIUMF were performing well after 6 months of use; no damage was reported.

Brown and Cost reported experiments conducted at LANL with reactor neutron irradiation of NdFeB [14, 15] and SmCo [16] samples under various conditions of temperature and external field. Long irradiations at relatively low fluxes were used to produce substantial doses; the dose rate was constant and used to estimate the dose. In 1987 they presented data [15] showing the demagnetization as a function of magnet aspect ratio, as is presented here in Chapter 3 for a different range of geometries.

More recently, Ito *et al.* presented in 2001 [6] and 2003 [7] data on the demagnetization of NdFeB and SmCo magnets of various grades and sizes, exposed to 200 MeV protons. Samples were measured by passing the magnet through a stationary coil and integrating the current generated, and the dose was measured with an ionization chamber. Additionally, they demonstrated that radiation-damaged and subsequently remagnetized samples behaved in the same way as new samples. Magnets which were thinner in the direction of magnetization were shown to be more susceptible to damage than thicker samples.

Other experiments have been reported which were less relevant to the current application. Talvitie *et al.* in 1991 [17] reported on damage to NdFeB magnets irradiated with 20-MeV protons. Okuda *et al.* [18] who reported on electron and gamma irradiation of magnet samples, which produced substantially less damage than proton/neutron radiation.

A literature search did not reveal any studies measuring radiation damage in quadrupoles. Since this is the key concern for pRad, a set of experiments were conducted to specifically address damage in quadrupoles.

Chapter 2

First Experiment

2.1 Overview

To study the demagnetization of PMQs under controlled conditions, a Halbach quad was intentionally irradiated with protons and spallation neutrons in a setup similar to that encountered in the pRad magnifier, and the magnetic field was measured as a function of dose.

The material in this section has been accepted for publication in Review of Scientific Instruments (Danly *et al.* [19]). In most of this document, doses are given as proton counts; this is the unit most convenient for proton radiography applications as it can be used directly to estimate the lifetime of magnetic lenses. Key data and plots give doses in Gray as well to enable comparison with other literature.

The objective of the experiment was to determine how much dose was required to render a PMQ lens unusable for imaging, and, by ensuring roughly symmetric irradiation, to rule out the possibility that the nonuniform damage seen in the pRad lenses might have been caused by poorly-steered proton beams impinging on the

magnet segments during tuning.

Irradiation and measurements were conducted in Area C at the Los Alamos Neutron Science Center accelerator. The magnet was mounted on a table in the beamline, downstream of a tungsten alloy cylinder. The experiment setup is illustrated in Figures 2.1 and 2.2 and will be discussed in this chapter.

Knowing only that damage was seen in the magnifiers after several months of regular usage, the decision was made to start with small doses and increase the increments until effects were observed.

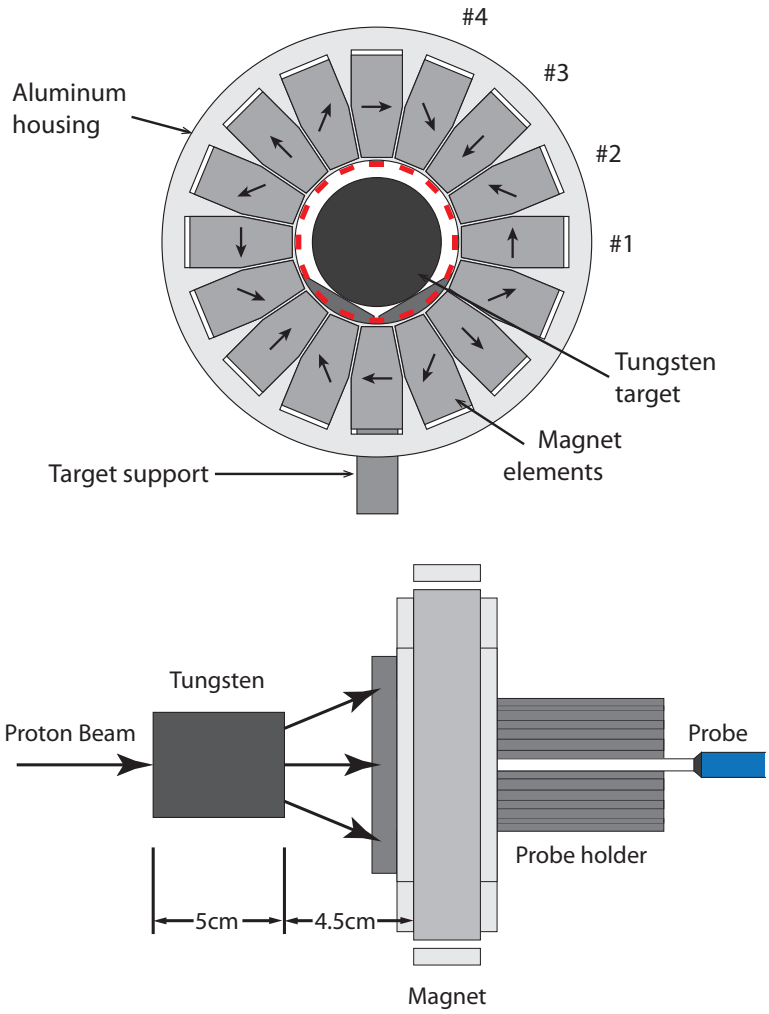

Figure 2.1: Configuration of magnet and target for experiment.

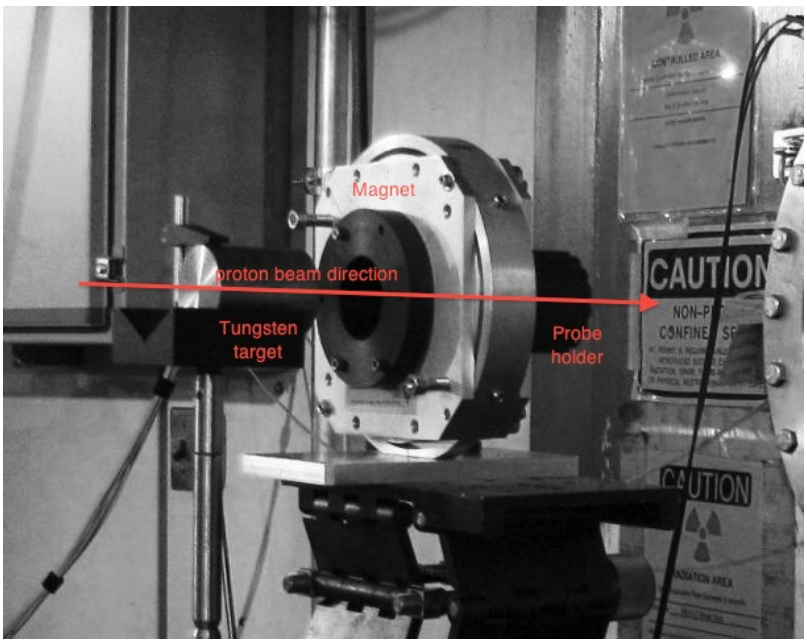

Figure 2.2: Experimental setup.

2.2 Samples and Instrumentation

2.2.1 Magnet

The PMQ used is a 16-segment Halbach quad which was originally constructed for an electron-radiography experiment[20]; it is shown in Figure 2.3. This PMQ is similar in design to those used in the pRad lenses, and constructed from the same material. The magnet is 2.4 cm thick with an inner (aperture) diameter of 5.08 cm and an outer diameter of 13.3 cm; the segments are irregular hexagons of Tridus Tri-Neo 38H NdFeB alloy[21].

This material has a specified remnant field of $1.23-1.30$ T and coercivity products $H_{cb} > 11.5$ kOe and $H_{cj} > 17$ kOe. The PMQ has a nominal field gradient of 0.42 T/cm and $L * B' = 1.0$ T

There are three "types" of segment with the magnetization axis aligned with, perpendicular to, or making a 45° angle to the long axis of the segment.

2.2.2 Radiation

The spallation target used was a machinable tungsten (MT-18C) cylinder 4 cm in diameter and 5 cm in length; this is essentially a zero-radian (no hole) pRad collimator. The target was mounted on a standard 2" aluminum optical v-block atop an optical post and positioned approximately 4.5 cm from the upstream face of the magnet.

The total proton dose delivered was determined with a calibrated integrating current transformer (ICT) on the pRad beamline. This proton count was later used to calculate the energy deposited in the magnet material using MCNPX.

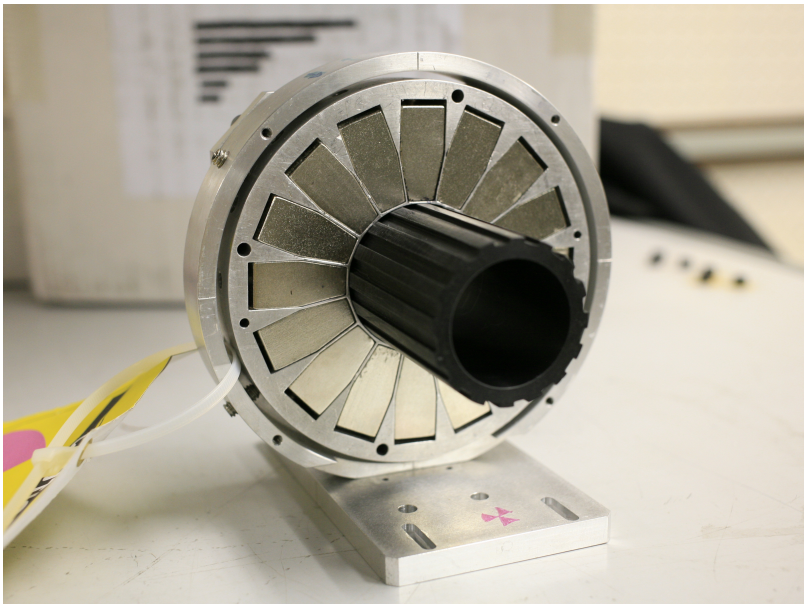

Figure 2.3: PMQ used for experiment, with cover removed and probe holder installed

The accelerator is capable of delivering 800 MeV protons at $> 100\mu A$ to this area but the pulse size was limited in order to ensure the accuracy of the integrated current transformer measurements.

2.2.3 Instrumentation

Initial measurements were made by David Barlow in 2009 using a rotating coil inserted in the aperture of the PMQ. The dose-dependent dataset presented here was collected in-situ between irradiations with a Hall-effect probe. The probe was positioned using a plastic holder mounted on the magnet, with slots at the tip of each magnetic element. This arrangement is visible in Figure 2.3.

A LakeShore model HMMT-6J04-VF transverse probe with a specified accuracy of $\pm 0.1\%$. The probe holder was, designed with all slots tangent to the circle, mean-

ing that $\mathbf{B} \cdot dA$ was near zero in the portions of the magnet where the field was tangent. Because of this, the relative error in these measurements was so large ($\sim 50\%$) that the data was not used for the final analysis.

At the end of the irradiation experiment, the PMQ was moved to the magnet lab and mapped with a rotating coil to determine magnetic multipole moments. These are discussed in the Results section below. The magnet was then disassembled and the individual segments were measured with a rotating sample Helmholtz-coil apparatus. This device was constructed by David Barlow based on the design in [22].

2.3 Experimental considerations

The experiment was conducted at room temperature and the energy deposited in the magnet by the proton beam was insufficient to raise the temperature substantially, so the temperature was not monitored. (The specific heat capacity of NdFeB is approximately 0.5 kJ/kg K and the maximum dose in the PMQ was approximately 2 kGy for a temperature increase less than 4 K.)

Safety procedures require the area to be surveyed after each beam delivery before entry and swept and secured when measurements are completed before more beam can be delivered. This limited the number of measurements which could be made. Additionally, the tungsten target used in the experiment became substantially activated (> 3 mSv/hr at 1 foot) as the dose increased; radiation safety considerations necessitated further delays. To provide some protection from this radiation, the target was mounted on a rail to allow it to be pulled into a shielded enclosure with a rope.

2.4 Data

The magnetic field data collected during the irradiations is presented in Figure 2.4 and in a more intuitive form in Figure 2.13. The numerical data is attached in the appendices. The analysis and error estimates are discussed in the next section.

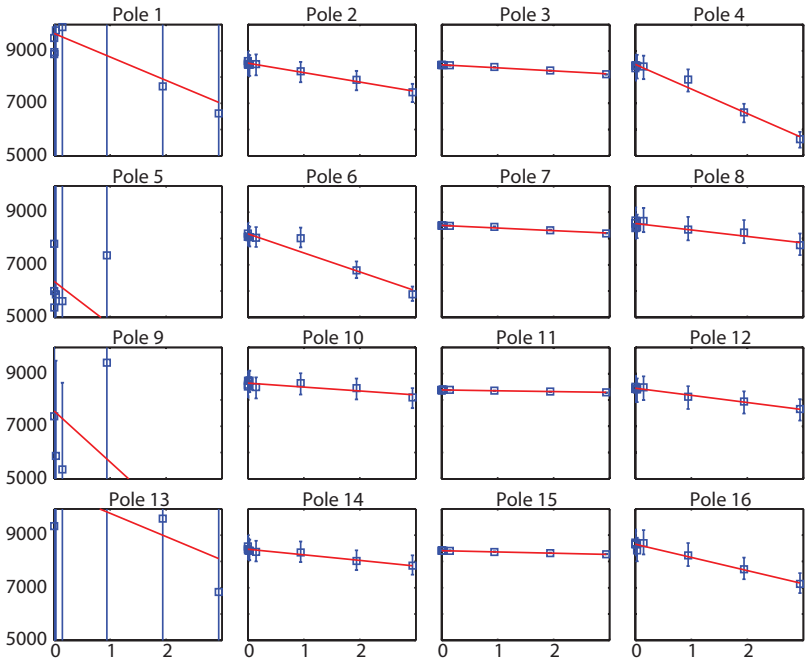

Figure 2.4: Magnetic field at each segment tip as a function of protons delivered. Vertical scale in Gauss, horizontal scale in 10^{13} protons.

2.5 Analysis

The analysis of this experiment consisted of calculation of the dose distribution in the PMQ, reduction of the magnetic field data, and the synthesis of the two.

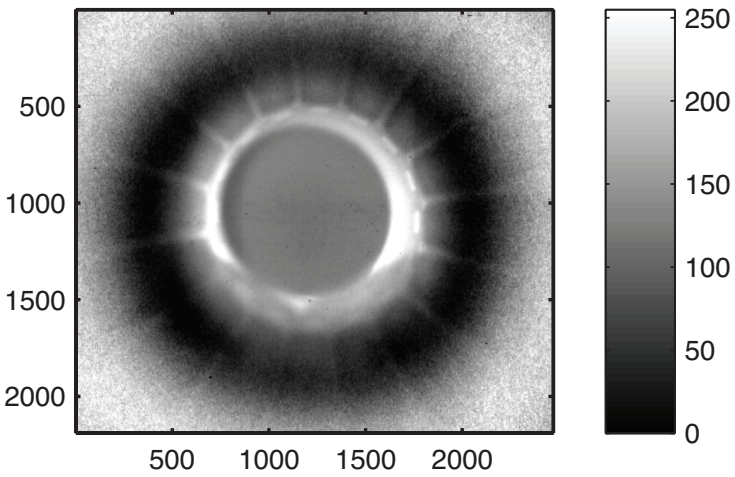

Figure 2.5: Flattened radiograph from image plate placed downstream of the magnet. X and Y scale in pixels, Color scale arbitrary.

2.5.1 Dose estimation

The beam profile was measured using image plates (reusable film-like detectors) positioned upstream of the tungsten, between the tungsten and the magnet, and downstream of the magnet. One of these images is shown in Figure 2.5. A 2d gaussian beam profile (x, y, and cross term) was fitted to this image and used for the remaining calculations. A slight offset between the axis of the magnet and the tungsten target was also observed in this image and incorporated into the model.

A detailed model of the experiment geometry was constructed in MCNPX; sections are shown in Figure 2.6. The model included accurate magnet geometry and material composition, and protons and neutrons were tracked in full Monte Carlo mode. A 2D mesh tally with 1mm resolution encompassing the volume of the magnet material provided dose (energy deposition) information. 3D mesh tallies of flux

in the volume including the tungsten target and magnet provided debugging information. The MCNPX distribution was then multiplied by the number of protons delivered to produce a map of the dose in the magnet; this is shown in Figure 2.7.

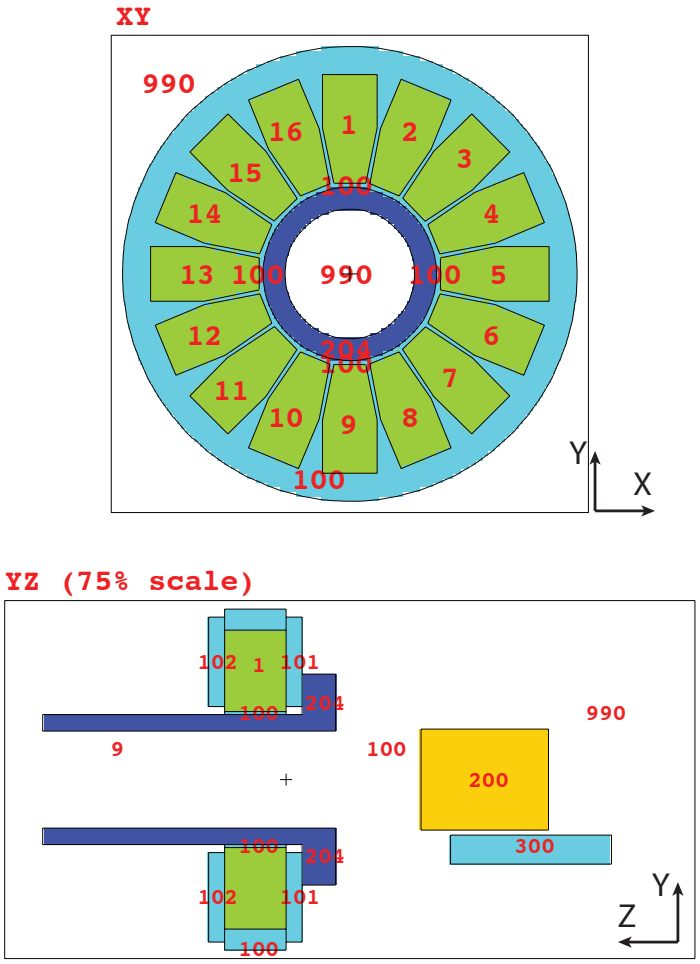

Figure 2.6: MCNPX geometry plotted in magnet plane (top) and vertical plane (bottom).

The dose in the magnet was position dependent, with the highest dose on the inner edge of the bottom segment. This area received a dose of approximately 1.7 kGy. The asymmetric dose distribution is partially due to misalignment of the beam and partially because of neutron production in the aluminum V-block holding the target.

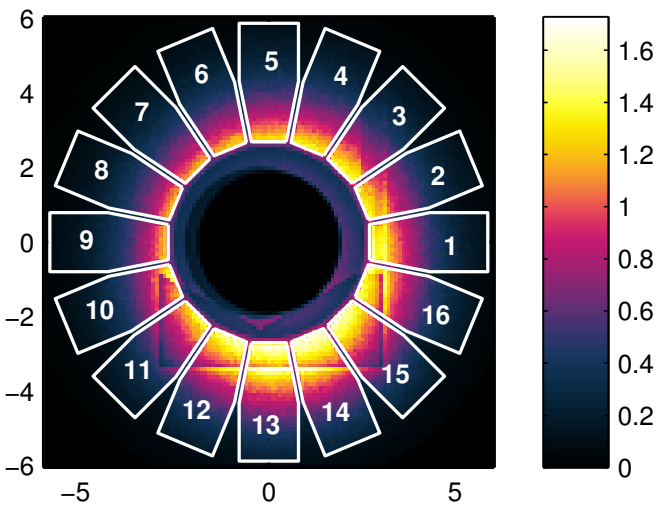

Figure 2.7: Energy deposition in magnet from MCNPX. X and Y scales in cm, color scale in kGy.

2.5.2 Magnetic field data

The direction of the B-field within the aperture of the PMQ varies with position and so the angle between the B-field and active area of the probe must be taken into account to correctly measure field strength. This calculation was performed in Matlab. Rotational tolerance of the probe in the holder slot was also used to estimate the error bars shown in Figure 2.4.

Rotational alignment of the probe holder to the magnet assembly within the tolerances of the mounting holes was by observation and was not perfect. This was corrected by fitting the initial (undamaged) quadrupole field strength to a sinusoid, and subtracting the phase shift. The angular offset was 1.5 degrees. The fit is shown in Figure 2.8.

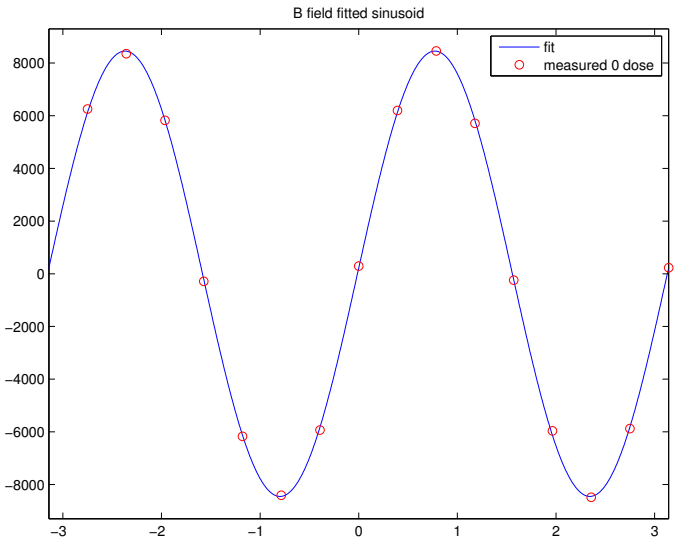

Figure 2.8: Zero-dose initial measurement compared to sinusoidal expected form. Vertical scale in cm, horizontal scale in radians.

The field of the assembled PMQ was mapped when the magnet was purchased

(2004), after completing the irradiation, and after remagnetization. These data provided the multipole moments of the lens which will be discussed later.

Finally, the magnet was disassembled and the individual segments measured using the rotating sample mapper described above. This provided high-accuracy measurements of the end state of the magnet elements, and these data were used to fit the tangential field segments.

The coercive field strength in the magnet was previously calculated by David Barlow using the Opera code and is shown in Figure 2.9.

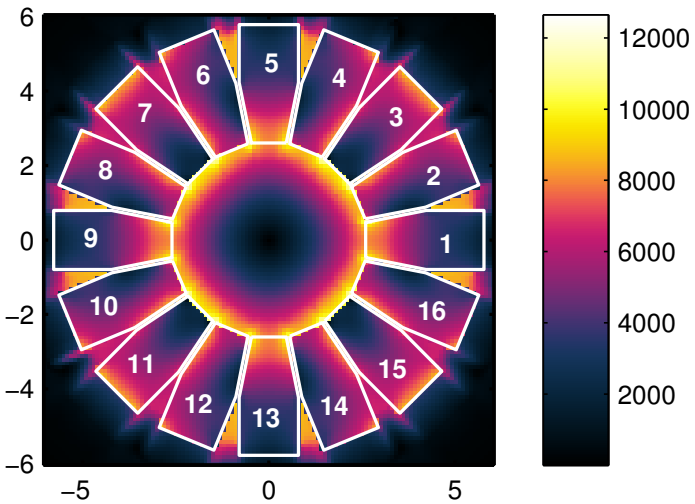

Figure 2.9: H_{mod} from Opera. X and Y scales in cm, color scale in Oersted.

2.5.3 Synthesis

The calculated coercive field and dose maps were multiplied in Matlab to produce an image showing where the damage will occur, shown in Figure 2.12, and this product

is referred to as $k(x, y)$. This compares favorably to the change in magnetic field in the PMQ as the dose is increased (Figure 2.13).

Attempts to determine a quantitative relationship between coercive field, dose, and susceptibility to demagnetization from the variation among like segments in the PMQ was unsuccessful.

2.6 Results

Individual magnet segments in the PMQ exhibited a loss of magnetization as expected. The flux loss was roughly linear to 80% demagnetization. The average demagnetization as a function of dose is shown in Figure 2.10.

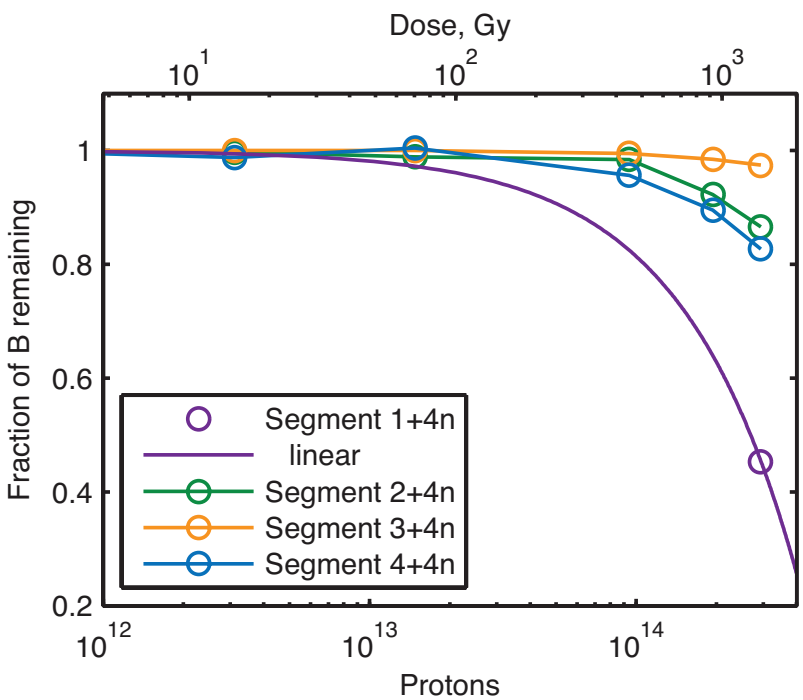

Figure 2.10: Damage as a function of dose, averaged over like segments.

The tangential field segments demagnetized significantly faster than the poles. This produced a deviation from the quadrupole nature of the field and an increase in higher-order multipole moments. These are shown in Figure 2.11.

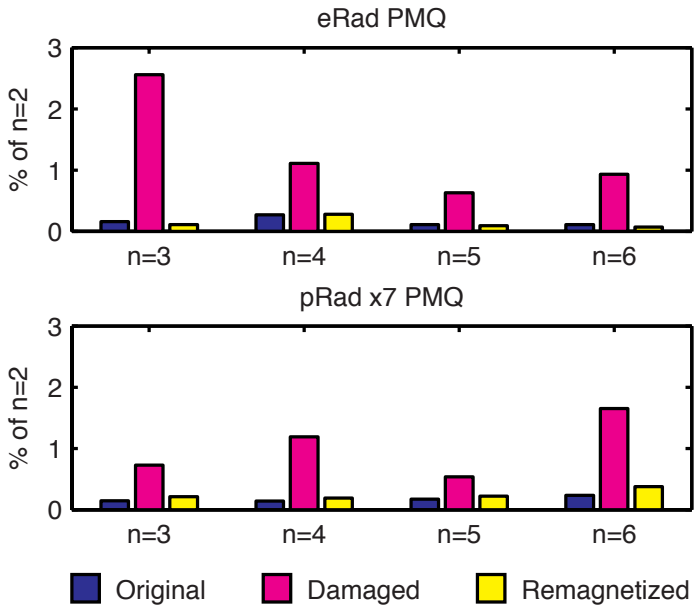

Figure 2.11: Higher-order multipole moments increased by radiation damage

Susceptibility to demagnetization was strongly correlated with the product of coercive field and radiation dose. This comparison is shown in Figures 2.12 and 2.13.

Despite a relatively uniform radiation dose, the PMQ tested exhibited nonuniform damage. The segments magnetized tangent to the aperture were demagnetized significantly faster than the poles. Therefore, the dose required to reduce the pole-tip field is not sufficient to estimate the useful life (time between remagnetizations) of a permanent magnet lens. Instead, demagnetization should be estimated based on the expected dose and the coercive field and permanence coefficient in the tangential field segments. For high-dose applications, more radiation-resistant magnet materials should be investigated.

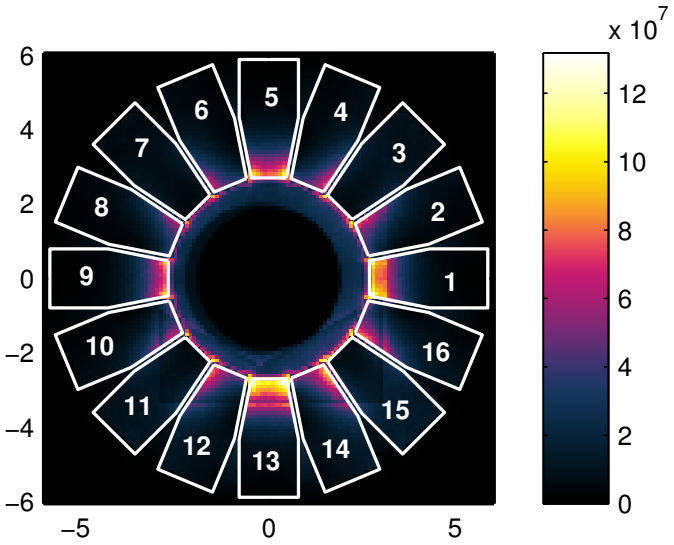

Figure 2.12: Product of H_{mod} and Dose. X, Y scales in cm, color scale in arb. units.

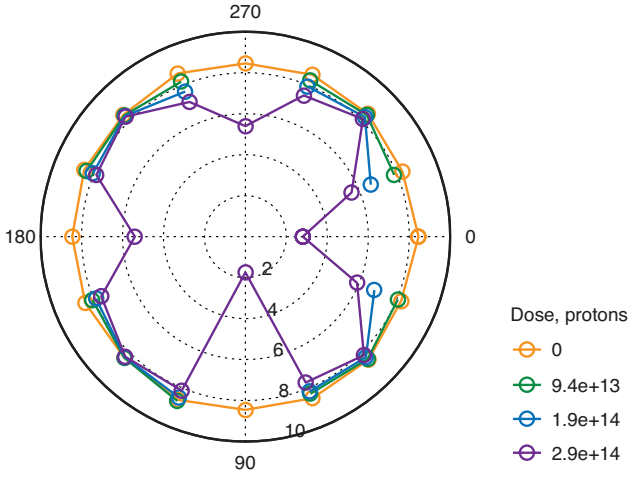

Figure 2.13: Plot of final field strength as a function of angle. Radial scale in kGauss.

Chapter 3

Second Experiment

3.1 Overview

The demagnetization in the PMQ was determined to be inherent to the configuration, and essentially unavoidable in the current pRad optics design. It was therefore decided to study the effect in more detail and supplement the existing literature with information about the material used in the pRad magnets - NdFeB 38H - and SmCo, with a view towards a potential redesign of the magnifier lens.

This experiment was similar to those performed by Ito and Talvitie and discussed in Section 1.4. Sample sizes were consistent with Ito but different alloys were chosen.

3.2 Samples and Instrumentation

3.2.1 Radiation

In contrast to the first experiment, magnet samples were irradiated directly with the 800-MeV proton beam.

3.2.2 Magnet characteristics

Magnet samples were ordered in various thicknesses and materials, with multiple samples of each. The magnets were cylindrical, 10 mm in diameter and in thicknesses of 1, 2, 3, 4, 8, and 16 mm. The materials used were Neodymium-Iron-Boron NdFeB-38H and Samarium-Cobalt Dexter S2630, which are used in the existing pRad magnifiers and under consideration for a redesigned lens, respectively. The samples were assigned 3-digit codes for identification, with the first letter N or S to denote the material (Neodymium or Samarium), the second character indicating the thickness ("A"=16 mm) and the third to differentiate identical samples. These will be used to refer to individual samples in plots and data tables. The samples irradiated in the experiment are shown in Figure 3.1.

Magnet samples were held in low-density mounts made of paper and foam to avoid interference with the proton beam and minimize production of secondary particles (n, gamma, etc.). The mounts were designed to hold even the thinnest samples on edge, so that the beam would pass along the direction of magnetization and to ensure accurate measurements in the Helmholtz coils. These mounts were placed on a motorized linear stage mounted in the beamline to allow multiple samples to be irradiated without entering the area. A mounted magnet is shown in Figure 3.2.

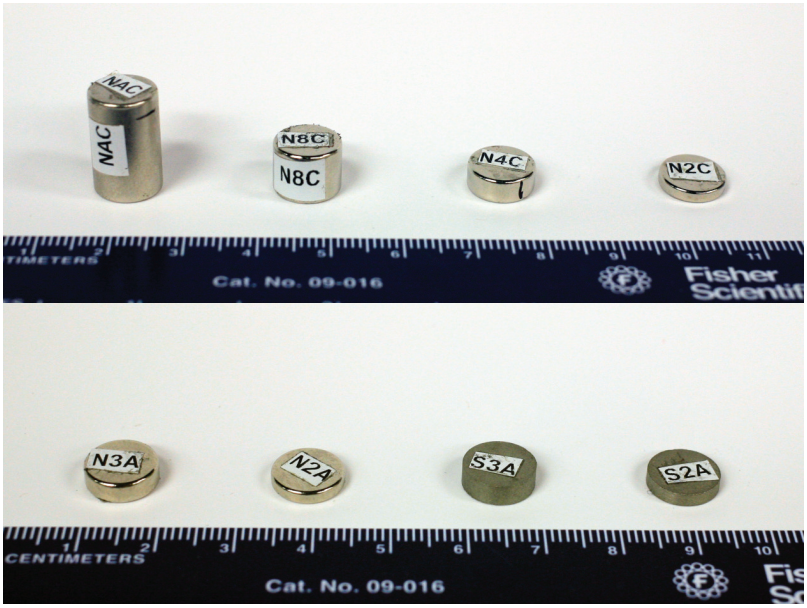

Figure 3.1: Magnet samples. Top: First batch, NdFeB in thicknesses of 16, 8, 4, and 2 mm. Bottom: NdFeB and SmCo in 3 and 2 mm each.

3.2.3 Instrumentation

The magnetic moment of the samples was measured between irradiations using the rotating sample Helmholtz coil device described above in Section 2.2.

Proton count was estimated based on the beam current and the number of pulses (time). Because of an upgrade to the data acquisition system, the integrating current transformer used previously was not calibrated and exact proton counts were unavailable.

The experiment was conducted in a secure area; the setup was not photographed.

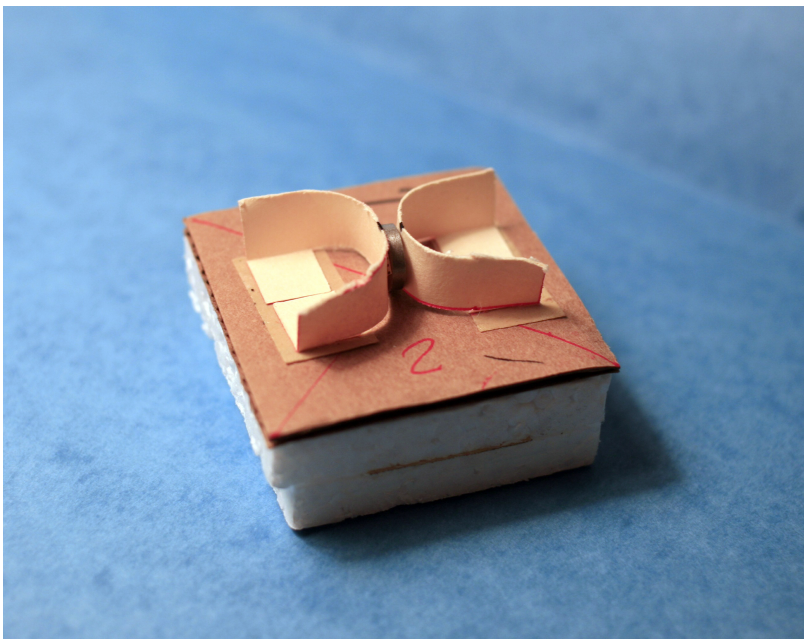

Figure 3.2: Magnet sample in paper and foam mount.

3.3 Data

Data tables are attached in the appendix; plots follow in the Results section.

3.4 Analysis

3.4.1 Dose analysis

Dose estimates were generated using a combination of the proton flux monitor (integrating current transformer) and an imaging phosphor placed on the beam pipe cover downstream of the magnet samples. The phosphor images were corrected for distortion using an affine transformation mapping them to a known grid; this allowed the relative positions of the magnets and beam to be measured in real-world

coordinates. Sample images are shown in Figure 3.3 and Figure 3.4.

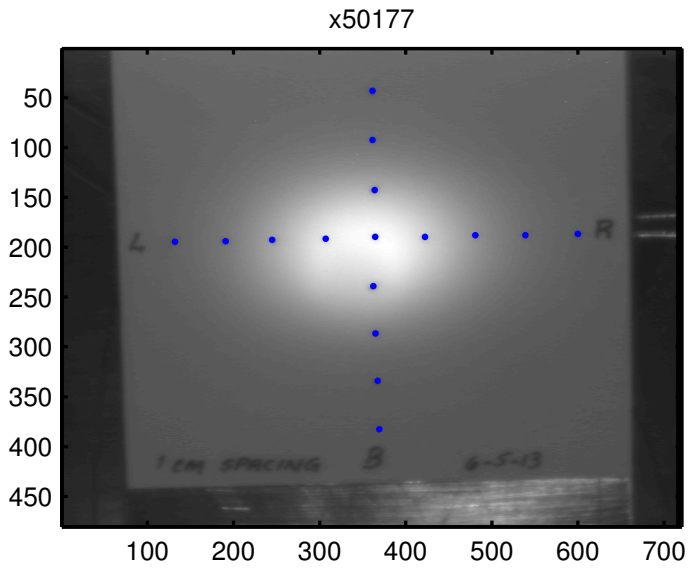

Figure 3.3: Raw phosphor image of NAC sample. Scale in pixels.

Because the problem geometry was simpler than in the first experiment, conversion from proton flux to dose (Gy) was computed manually. The NIST PSTAR database[23] gives proton stopping powers for various materials. The database does not include neodymium or boron, but it includes molybdenum and carbon which differ from the materials of interest by only 1 proton; these were used. The values given are Mo 1.497, Fe 1.659, and C 2.051 MeV cm^2/g. Weighting by atomic fraction in the magnet material, the average stopping power for NdFeB is approximately 1.663 MeV cm^2/g. For even the thickest sample, the protons lose only 20 MeV of their initial energy (800 MeV), so the change in stopping power is negligible, and the single energy calculation below is valid. The energy lost by the proton as it passes through the magnet is mostly absorbed by the magnet, so the dose is then given by:

$$\text{Dose (kGy)} = \frac{\text{protons}}{\text{cm}^2} \cdot \frac{1.663 \text{ MeV} \cdot \text{ cm}^2}{\text{g}} \cdot \frac{1.602 \times 10^{-13} \text{ J}}{\text{MeV}}$$

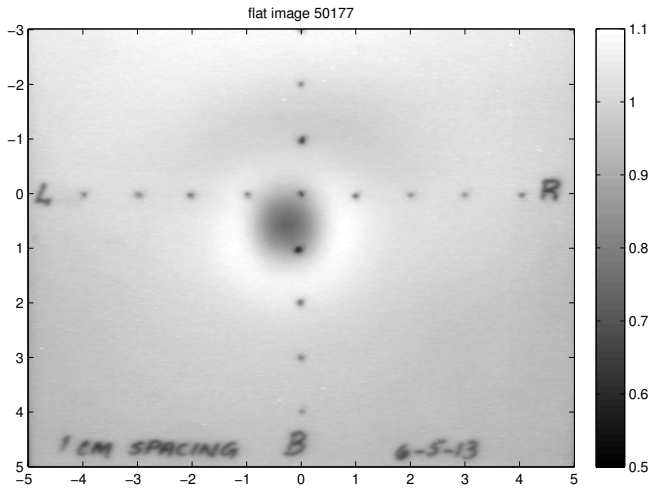

Figure 3.4: Image dewarped, mapped to real-world coordinates, and divided by beam profile. X and Y scales in cm, color scale is intensity ratio.

This dose calculation was verified with an MCNPX simulation of the experiment using the beam profile measured in the next section.

3.4.2 Beam profile

The beam profile was measured using the dewarped phosphor image, which was used to fit a 2d Gaussian as in Figure 3.5. The Gaussian was normalized and then numerically integrated over the measured area of the magnets (Figure 3.6) to calculate the fraction of protons delivered that actually passed through the magnet. The numerical integration was verified analytically for a centered region and the error was $< 0.5\%$.

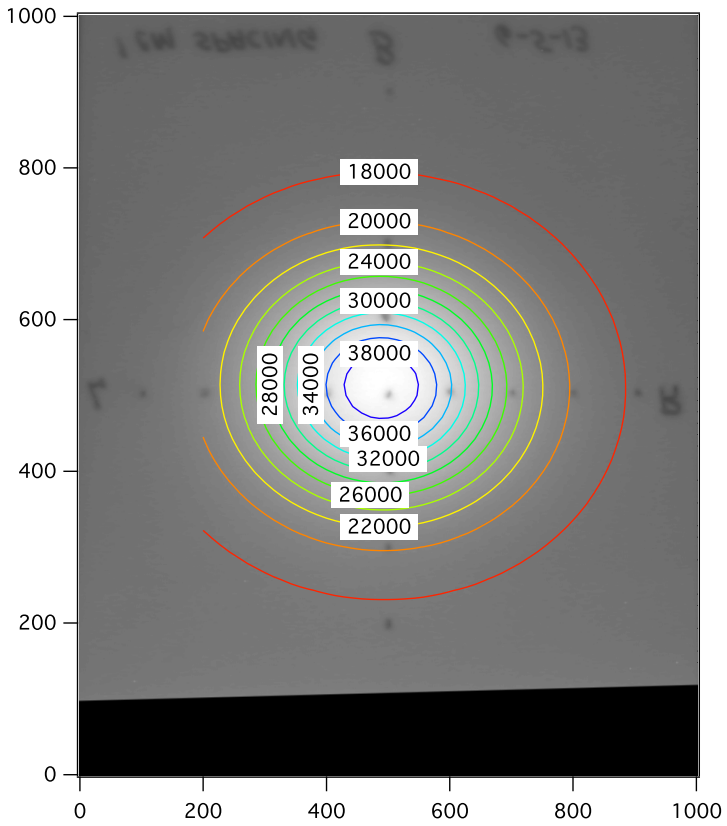

Figure 3.5: Gaussian fit to dewarped phosphor image. Scale is 0.1 mm pixels.

3.4.3 Droop

The hydraulic table on which the magnet samples were mounted for irradiation suffered an unexpected, slow leak and therefore dropped gradually over the course of the experiment. The positions of the magnets were measured before the first set of samples was irradiated, and then when the samples were swapped for the second set. This revealed that the table had fallen approximately 7 mm. The table was returned to the correct height and wedged to keep it in place for the remaining two sets of measurements.

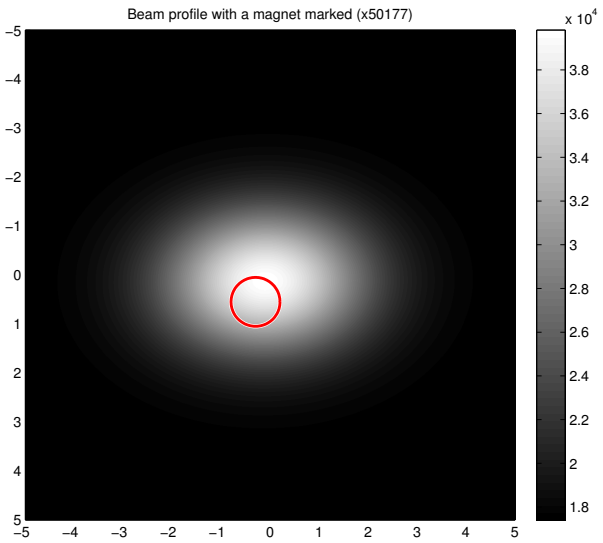

Figure 3.6: Gaussian with magnet location for integration. X and Y scales in cm.

Assuming that the table height decreased at a constant rate (linear), the position of the magnet for each irradiation was estimated with a linear fit between the two sets of position measurements at known times. This is used to correct the dose data.

A second set of N2-type samples were irradiated after the table was wedged, and these were used to validate the dose correction technique. The N3A and N3D samples fell between the N2C and N4C curves, as expected (Figure 3.7). The N2A and N2E samples both exhibited substantially faster demagnetization than the N2C sample; the reason for this inconsistency is not known.

3.4.4 Error Analysis

The dominant source of error in the experiment was the uncertainty in the position of the magnets relative to the beam. To estimate the error bars, the gaussian dose

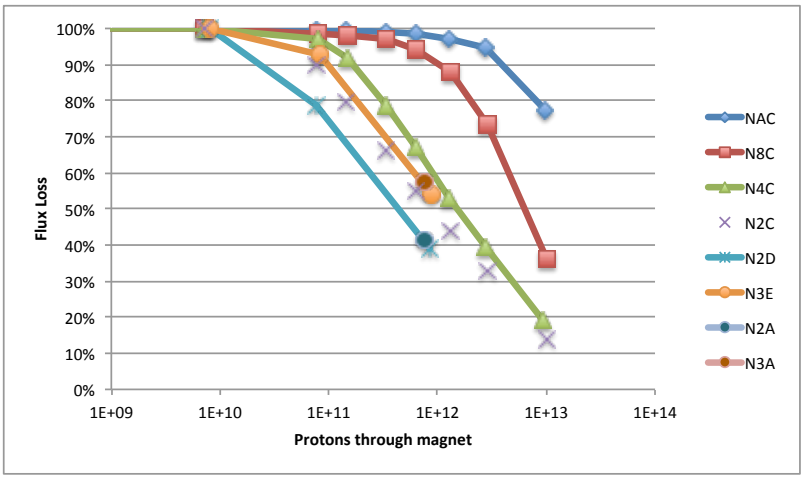

Figure 3.7: Demagnetization as a function of proton count for all NdFeB samples.

integration described above was performed with 1 mm offsets in each direction; the change in estimated dose determines the error. Adding these errors over the course of the experiment (because the magnets were moved between irradiations) gives an estimated dose error from 3% at the low dose side of the curve to 13% on the last measurement. This estimate does not take into account variation in the accelerator beam current.

The magnet mapping equipment used averages multiple measurements and tests showed the random error to be less than 1% so it is ignored here. Systematic error was not investigated.

3.5 Results

Flux loss in the samples tested was initially linear, transitioning to an exponential (logarithmic) behavior for flux loss over 20%. Flux loss greater than 90% was not reached but the behavior is expected to be consistent with the literature. Demagnetization as a function of dose is shown in Figure 3.8.

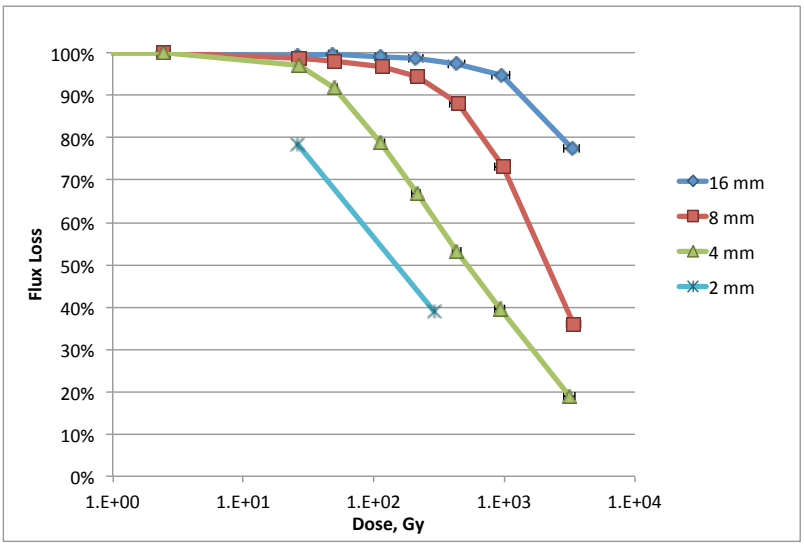

Figure 3.8: Demagnetization as a function of dose for selected samples

The dose required to demagnetize samples by 20% (D20) is significantly lower than that for similar samples reported in Ito. For the 2 mm thickness samples of N32Z and N48, Ito reported D20 of 2.3×10^4 and 5.1×10^2 Gy respectively. The N38 sample tested here had a coercivity in between those of the N32Z and N48 and exhibited 20% demagnetization at a calculated dose of 1.1×10^2 Gy. This is shown in Figure 3.9. Clearly, further study is required to fully understand the parameter space.

Samples which were thinner in the direction of magnetization (and therefore had lower permanence coefficient) were more susceptible to damage. The relationship

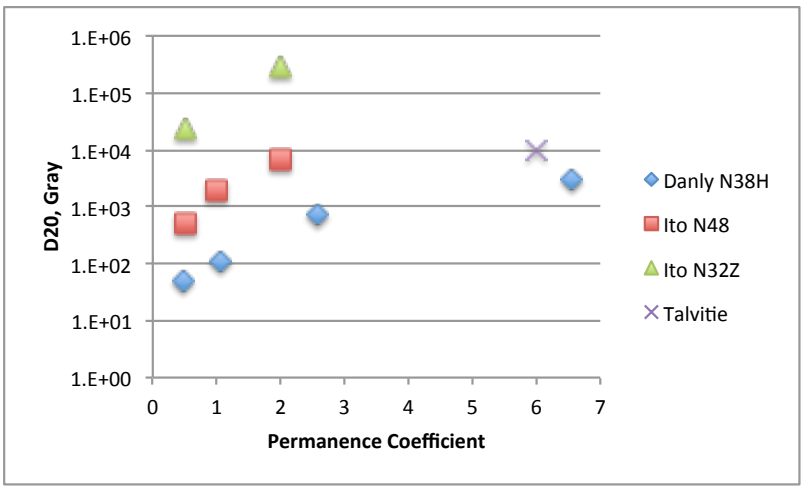

Figure 3.9: D20, dose to demagnetize by 20% as a function of permanence coefficient. Compared for present data, Ito *et al.* [6] and Talvitie *et al.* [17]

between aspect ratio of the magnet and $D20$ is shown in Figure 3.10. It is consistent with the relationship previously published.

None of the samarium cobalt magnets tested exhibited a measurable decrease in strength over the course of the experiment. Based on the damage seen in the thin samples of NdFeB at low doses, it is estimated that SmCo is at least a factor of 10^3 more resistant to radiation. As a result of this data, the LANL pRad 7X magnifier has been redesigned to use SmCo magnets and is currently being reconstructed. The reason for the increased radiation hardness of SmCo is not known.

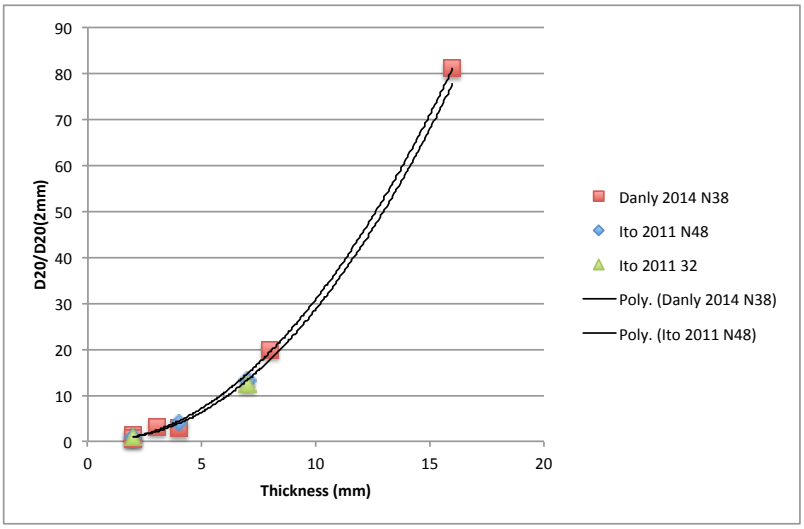

Figure 3.10: D20 normalized to 2mm sample for various samples.

Chapter 4

Conclusions

In the first experiment, the conclusion was reached that permanent magnet quadrupole lenses exhibit nonuniform radiation-induced demagnetization as a result of the variations in coercive field and geometry within the PMQ. This results in an increase in non-quadrupole field components and a loss of imaging quality in radiography applications faster than would be expected based on the loss of pole-tip field alone. This effect is determined to be inherent to the quadrupole configuration, and not easily mitigated. Therefore, the use of more radiation-tolerant materials is advised.

The second study provided quantitative data on the dose required to demagnetize samples of magnetic materials used in pRad lenses. The data showed the propensity for demagnetization is related to the aspect ratio of the magnet, with thicker samples more resistant to damage. This is consistent with previously reported results. Samarium cobalt is confirmed to be far superior to Neodymium-iron-boron for high-dose radiography applications. Damage was seen at lower doses than expected in NdFeB but no demagnetization was measured in even the thinnest samples SmCo at doses up to 1 kGy or delivered proton counts of 10^{13}. This material is recommended for use in future radiography applications.

Chapter 5

Continuing and Future Work

Efforts to understand the radiation environment and damage processes in magnetic lenses are ongoing. Dosimetry measurements at various points on the LANL 3X magnifier were made using CR-39 track-etch plastic in early 2014 but the dose was too high to be read using the traditional track-counting technique. Information may be extracted with further calibration or a shorter exposure.

In May 2014, a proton radiography system was commissioned at GSI in Darmstadt, Germany using NdFeB magnets. The initial tuning campaign suggested that the magnetic field strength in these lenses is lower than expected and an effort is being made to understand why. The dose to the magnets was characterized using radiochromic film and this data is being examined.

The 7X magnifier at LANL pRad has been redesigned to use samarium-cobalt magnets and the new lenses are presently being constructed. This should eliminate the problems and allow continuous use of the magnifier. Finally, sufficient data is available so that future work could produce an integrated model of radiation damage in magnetic optics to allow easy estimation of damage and lifetime during the design phase.

The existing literature in this area is sparse and previous experiments seem to have been conducted, as this study was, to answer specific questions for specific applications. A comprehensive study of radiation-induced demagnetization, as a function of magnet material and grade, shape, temperature, and type and energy of radiation, would be a valuable addition to the body of scientific knowledge.

Appendices

A PMQ experiment **4**

B Material sample experiment **5**

Appendix A

PMQ experiment

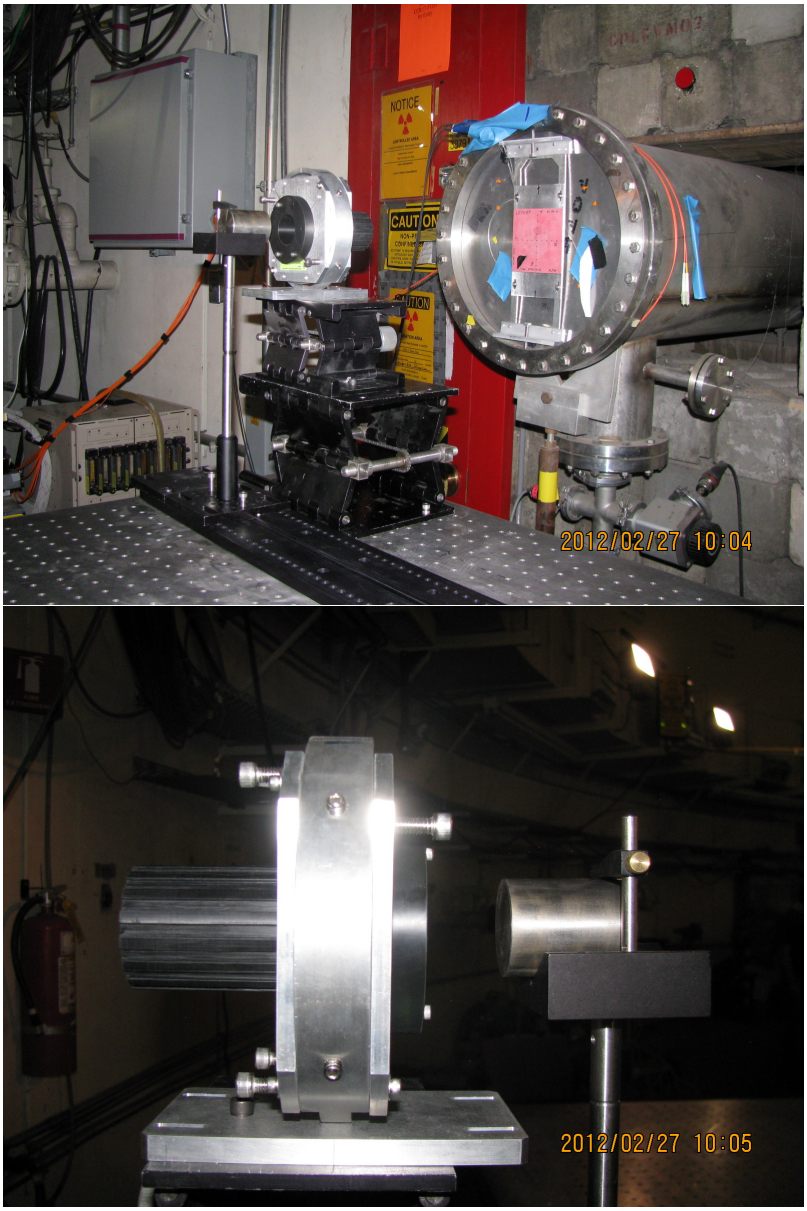

Figure A.1: Additional photos showing experimental setup.

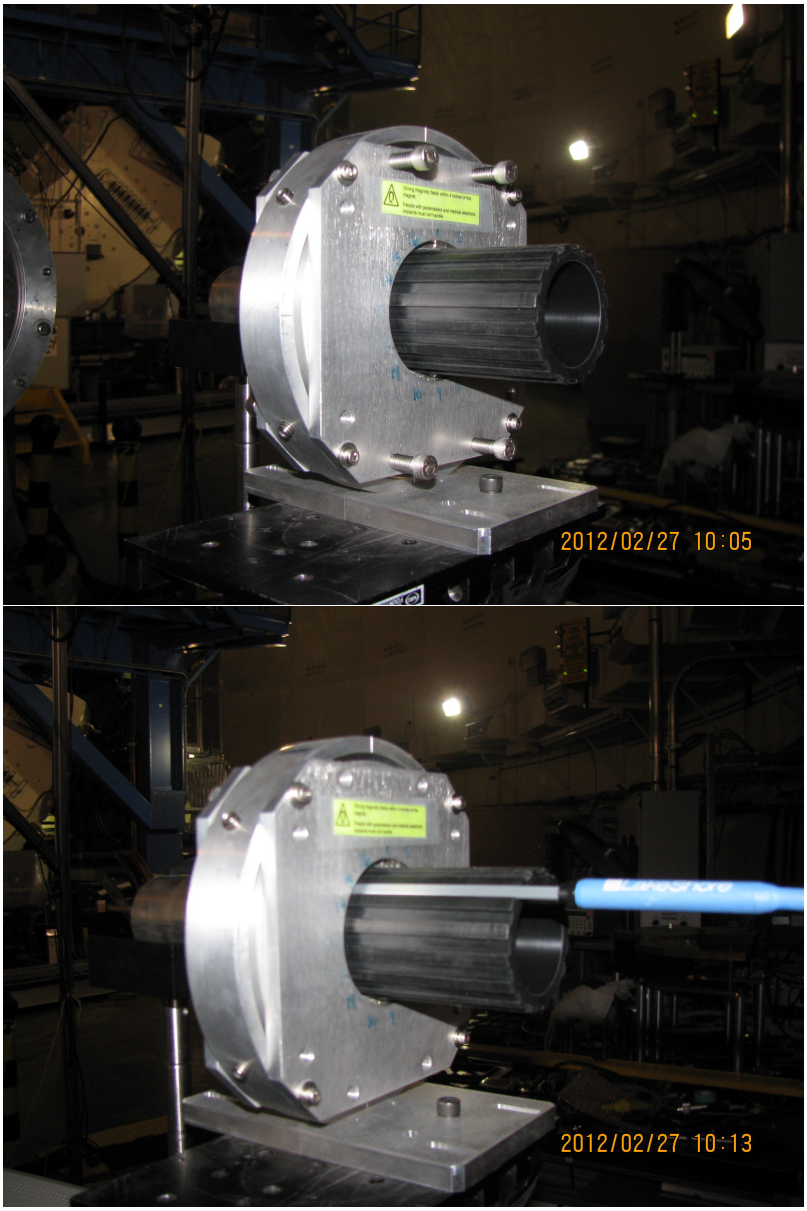

Figure A.2: Probe inserted into PMQ

A.1 Data

Table A.1: **B field in PMQ (Gauss) as a function of dose**

Segment Type	#	Dose, protons 0	2E+10	2.2E+11	3.1151E+12	1.47951E+13	9.43E+13	1.94E+14	2.94E+14
0	1	294	275	277.5	303	307	330	237	205
1	2	6200	6274	6168.5	6172	6189	5989	5752.5	5407.5
2	3	8459	8454	8453.5	8452	8447	8382	8246.5	8105.5
1	4	5710	5773	5780	5773	5753	5412	4558.5	3859
0	5	-242	-186	-166.5	-182	-174	-228	19	77
-1	6	-5966	-5874	-5878.5	-5864	-5849	-5837	-4944.5	-4281.5
-2	7	-8487	-8486	-8484	-8482	-8478	-8436	-8309	-8186.5
-1	8	-5879	-5750	-5947	-5770	-5935	-5712	-5635	-5305.5
0	9	229	366	154.5	182	166	292	75.5	54
1	10	6253	6201	6362	6366	6186	6296	6156.5	5899
2	11	8353	8384	8377.5	8385	8381	8352	8316	8285.5
1	12	5824	5774	5763.5	5754	5809	5562	5437	5243
0	13	-290	-328	-321.5	-328	-327	-389	-298.5	-212
-1	14	-6175	-6245	-6137	-6129	-6096	-6078	-5843	-5712.5
-2	15	-8409	-8407	-8406	-8405	-8401	-8358	-8313	-8269
-1	16	-5933	-5972	-5925.5	-5766	-5955	-5636	-5275.5	-4894.5

Table A.2: **Individual segments measured after damage and after remagnetization. Units of Gauss.**

Segment	Damaged	Remagnetized
1	12.268	13.349
2	12.907	13.265
3	13.345	13.414
4	12.447	13.199
5	11.494	13.232
6	12.698	13.338
7	13.166	13.254
8	12.915	13.23
9	12.645	13.316
10	13.176	13.519
11	13.23	13.315
12	12.978	13.131
13	12.507	13.228
14	12.911	13.245
15	13.173	13.254
16	13.021	13.23

A.2 Listing of MCNP deck

```
Title: Demag MCNPX Deck v1.2
c cell cards
c
c magnet elements
1   60  -10 -401:-402   imp:n=1 imp:h=1 $ Magnet elements
2   like 1 but trcl=302 u=0 imp:n=1 imp:h=1
3   like 1 but trcl=303 u=0 imp:n=1 imp:h=1
4   like 1 but trcl=304 u=0 imp:n=1 imp:h=1
5   like 1 but trcl=305 u=0 imp:n=1 imp:h=1
6   like 1 but trcl=306 u=0 imp:n=1 imp:h=1
7   like 1 but trcl=307 u=0 imp:n=1 imp:h=1
8   like 1 but trcl=308 u=0 imp:n=1 imp:h=1
9   like 1 but trcl=309 u=0 imp:n=1 imp:h=1
10  like 1 but trcl=310 u=0 imp:n=1 imp:h=1
11  like 1 but trcl=311 u=0 imp:n=1 imp:h=1
12  like 1 but trcl=312 u=0 imp:n=1 imp:h=1
13  like 1 but trcl=313 u=0 imp:n=1 imp:h=1
14  like 1 but trcl=314 u=0 imp:n=1 imp:h=1
15  like 1 but trcl=315 u=0 imp:n=1 imp:h=1
16  like 1 but trcl=316 u=0 imp:n=1 imp:h=1
c
c tungsten target
200 74 -10 -410           imp:n=1 imp:h=1 trcl=400 $ W Cylinder
c
c Probe holder
204 4 -1.42 (-501:-502) 503    imp:n=1 imp:h=1
```

```
c
c target holder
300 13 -2.7 -301:-302:-303:-304 imp:n=1 imp:h=1 trcl=400
305 316 -8 -305 imp:n=1 imp:h=1 trcl=400 $ minipost
c
c aluminum shell and faceplates
100 13 -2.7 -311 312 #1 #2 #3 #4 #5 #6 #7 #8
      #9 #10 #11 #12 #13 #14 #15 #16 imp:n=1 imp:h=1
101 13 -2.7 -313 315 imp:n=1 imp:h=1 $ Faceplate
102 like 101 but trcl=322 imp:n=1 imp:h=1
c
c test objects
c 601 74 -19.1 -801 imp:n=1 imp:h=1 $test box
c 18 74 -19.1 -500 imp:n=1 imp:h=1 $ test sphere
c
c problem bounds
990 0 -888 #1 #2 #3 #4 #5 #6 #7 #8 #101 #100 #102 #305 &
           #9 #10 #11 #12 #13 #14 #15 #16 #200 #204 #300 &
                              imp:n=1 imp:h=1
999  0 888                    imp:n=0 imp:h=0

c surface cards
401 ARB 0.469 2.667 0.000 0.795 4.290 0.000 -0.795 4.290 0.000
       -0.469 2.667 0.000 0.469 2.667 2.400 0.795 4.290 2.400
        -0.795 4.290 2.400 -0.469 2.667 2.400
       1234 1265 2673 3487 4158 5678
402 RPP -0.795 0.795 4.290 5.847 0.000 2.400
403 302 ARB 0.469 2.667 0.000 0.795 4.290 0.000 -0.795 4.290 0.000
```

```
       -0.469 2.667 0.000 0.469 2.667 2.400 0.795 4.290 2.400
        -0.795 4.290 2.400 -0.469 2.667 2.400
       1234 1265 2673 3487 4158 5678
404 302 RPP -0.795 0.795 4.290 5.847 0.000 2.400
409 PZ -7
C
C TUNGSTEN
410 RCC 0 0 -5.27435 0 0 -5 2 $ Cylinder for W
C
C TEST SPHERE
500 S 0 3 -1 1
801 RPP -1 1 3 4 3 9 $ Test box
C
C PROBE HOLDER
501 RCC 0 0 -1.9406 0 0 1.3056 4.1275 $ Probeholder-Flange
502 RCC 0 0 -0.6350 0 0 10.16 2.54 $ Probeholder snout
503 CZ  1.905 $ Probeholder bores
C
C TARGET SUPPORT
301 RPP -3.2824 -2.5966 -3.3109 -0.8166 -12.7244 -6.4244
303 RPP -0.1074 0.0577 -3.3109 -2.3279 -12.7244 -6.4244
302 ARB -2.59664 -3.31089 -12.72435 -2.59664 -0.81661 -12.72435
      -0.10744 -2.24409 -12.72435 -0.10744 -3.31089 -12.72435 -2.59664
      -3.31089 -6.42435 -2.59664 -0.81661 -6.42435 -0.10744 -2.24409
      -6.42435 -0.10744 -3.31089 -6.42435 1234 1485 5876 7326 4378 2156
304  ARB 0.05766 -3.31089 -12.72435 0.05766 -2.24409 -12.72435
      2.68910 -0.81661 -12.72435 2.68910 -3.31089 -12.72435 0.05766
      -3.31089 -6.42435 0.05766 -2.24409 -6.42435 2.68910 -0.81661
```

```
      -6.42435 2.68910 -3.31089 -6.42435 1234 1485 5876 7326 4378 2156
305 RCC -2.939542 -0.8166 -9.574  0 5.08 0  0.31  $ small post
C
c
311 RCC 0 0 0  0 0 2.4  6.6675  $ Aluminum disc
312 CZ 2.54  $ Bore
313 RPP -6.35 6.35  -6.35 6.35  -0.635 0.  $ Faceplate box in location
c 314 Reserved for intersection box
315 CZ  2.8575   $ Faceplate bore
c
C PROBLEM BOUNDS
888 RPP -7. 7. -7. 7. -16 11

c data cards
c
c translations
TR301 0.0 0.0 0.0 1.0 0.0 0.0 0.0 1.0 0.0 0.0 0.0 1.0
TR302 0.0 0.0 0.0 0.9239 -0.3827 0.0 0.3827 0.9239 0.0 0.0 0.0 1.0
TR303 0.0 0.0 0.0 0.7071 -0.7071 0.0 0.7071 0.7071 0.0 0.0 0.0 1.0
TR304 0.0 0.0 0.0 0.3827 -0.9239 0.0 0.9239 0.3827 0.0 0.0 0.0 1.0
TR305 0.0 0.0 0.0 0.0 -1.0 0.0 1.0 0.0 0.0 0.0 0.0 1.0
TR306 0.0 0.0 0.0 -0.3827 -0.9239 0.0 0.9239 -0.3827 0.0 0.0 0.0 1.0
TR307 0.0 0.0 0.0 -0.7071 -0.7071 0.0 0.7071 -0.7071 0.0 0.0 0.0 1.0
TR308 0.0 0.0 0.0 -0.9239 -0.3827 0.0 0.3827 -0.9239 0.0 0.0 0.0 1.0
TR309 0.0 0.0 0.0 -1.0 0.0 0.0 0.0 -1.0 0.0 0.0 0.0 1.0
TR310 0.0 0.0 0.0 -0.9239 0.3827 0.0 -0.3827 -0.9239 0.0 0.0 0.0 1.0
TR311 0.0 0.0 0.0 -0.7071 0.7071 0.0 -0.7071 -0.7071 0.0 0.0 0.0 1.0
TR312 0.0 0.0 0.0 -0.3827 0.9239 0.0 -0.9239 -0.3827 0.0 0.0 0.0 1.0
```

```
TR313 0.0 0.0 0.0 0.0 1.0 0.0 -1.0 0.0 0.0 0.0 0.0 1.0
TR314 0.0 0.0 0.0 0.3827 0.9239 0.0 -0.9239 0.3827 0.0 0.0 0.0 1.0
TR315 0.0 0.0 0.0 0.7071 0.7071 0.0 -0.7071 0.7071 0.0 0.0 0.0 1.0
TR316 0.0 0.0 0.0 0.9239 0.3827 0.0 -0.3827 0.9239 0.0 0.0 0.0 1.0
TR322 0. 0. 3.035
tr400 0.25 0 0
c
c materials
M4 012000 1 001000 2 016000 1 nlib=.66c hlib=.24h $ Delrin
M13 013000 1 $ Aluminium
M60 060000 2 026000 14 005000 1 nlib=.66c hlib=.24h $ NdFeB
c M74 074000 1 $ Tungsten
M74 074000 -0.95 028000 -0.035 029000 -0.015 $ tungsten MT-18C
M316 026000 -0.68 024000 -0.17 028000 -0.12 042000 -0.02 025000 -0.01 $ SS316
c
c problem definition
mode n h
lca
phys:n 810 $ neutrons up to 800 MeV
phys:h 810 $ protons up to 800 MeV
cut:n 1e8 0.001
c
c detector
c tir5:n 0. 0. 1.2 0. 0. 0. -1. 0. 8.5 0.
c FS5 -6 120i 6
c C5 -6 120i 6
c E5 1 99i 1000
c F4:N 401
```

```
prdmp j -30 j 1
print
c
c source
SDEF PAR=h ERG=800 DIR=1 VEC=0. 0. 1. X=D1 Y=D2 Z=-15 CCC=990
c x and y gaussians from image plate
SP1  -41 4.76 -0.50
SP2  -41 5.29 -0.30
nps 1e7 1
c
c
c other tallies
c mesh tally for edep, flux, etc
tmesh
 rmesh1:n flux
 cora1 -6. 60i 6.
 corb1 -6. 60i 6.
 corc1 -15 100i 10
 rmesh3
 cora3 -6. 120i 6.
 corb3 -6. 120i 6.
 corc3 0 2.4
 rmesh11:h flux
 cora11 -6. 60i 6.
 corb11 -6. 60i 6.
 corc11 -15 100i 10
endmd
c ring tally for energy spectrum
```

```
c ring tally for energy spectrum
c f15z:h -0.5 4.25 0
c e15 0.001 40i 800
c
c tally comments
fc1 neutron flux mesh 100 z-bins
fc3 energy deposition mesh 1 z-bin encompassing magnet volume
fc11 proton h flux mesh 100 z-bins
```

Appendix B

Material sample experiment

B.1 Data

Table B.1: **First batch of samples. Magnetic moment in uV*sm**

p, Increment	p, Cumulative	**N2C**	**N4C**	**N8C**	**N16C**
1	**1**	0.178	0.353	0.742	1.502
1.00E+11	**1E+11**	0.178	0.353	0.742	1.502
1.00E+12	**1.10E+12**	0.160	0.343	0.732	1.496
1.00E+12	**2.10E+12**	0.142	0.324	0.728	1.497
3.00E+12	**5.10E+12**	0.118	0.278	0.719	1.489
5.00E+12	**1.01E+13**	0.098	0.236	0.7	1.482
1.20E+13	**2.21E+13**	0.078	0.188	0.654	1.462
3.00E+13	**5.21E+13**	0.058	0.14	0.543	1.423
1.50E+14	**2.02E+14**	0.025	0.067	0.267	1.164

Table B.2: **Second batch of samples. Magnetic moment in uV*sm**

p, Increment	p, Cumulative	**N2A**	**N3A**	**S2A**	**S3A**
1	**1**	0.177	0.29	0.167	0.251
1.00E+11	**1E+11**	0.178	0.353	0.742	1.502
1.00E+13	**1.01E+13**	0.073	0.166	0.167	0.25

Table B.3: **Third batch of samples. Magnetic moment in uV*sm**

p, Increment	p, Cumulative	**N2D**	**N3E**	**S1C**
1	**1**	0.177	0.287	0.081
1.00E+12	**1.00E+12**	0.139	0.266	0.081
1.00E+13	**1.10E+13**	0.069	0.155	–

Table B.4: **Cumulative dose at various measurements (Gy)**

Increment	NA	N8	N4	N2
1	2.41E+00	2.45E+00	2.47E+00	2.43E+00
2	2.62E+01	2.66E+01	2.68E+01	2.63E+01
3	4.89E+01	4.97E+01	4.99E+01	4.93E+01
4	1.13E+02	1.15E+02	1.14E+02	1.14E+02
5	2.12E+02	2.16E+02	2.13E+02	2.15E+02
6	4.35E+02	4.45E+02	4.33E+02	4.43E+02
7	9.53E+02	9.78E+02	9.30E+02	9.73E+02
8	3.32E+03	3.42E+03	3.15E+03	3.41E+03

References

[1] N. S. P. King et al., Nucl. Instrum. Methods Phys. Research A **424**, 84 (1999).

[2] W. T. Buttler et al., Journal of Fluid Mechanics **703**, 60 (2012).

[3] F. E. Merrill et al., Rev. Sci. Instrum. **82**, 103709 (2011).

[4] T. Mottershead et al., Design and operation of a proton microscope for radiography at 800 MeV, in *Particle Accelerator Conference, 2003. PAC 2003. Proceedings of the*, volume 1, pages 702–704, IEEE, 2003.

[5] F. E. Merrill et al., AIP Conference Proceedings **1195**, 667 (2009).

[6] Y. Ito et al., Nucl. Instrum. Meth. B **183**, 323 (2001).

[7] Y. Ito et al., Nucl. Instrum. Meth. B **209**, 362 (2003).

[8] D. B. Barlow, R. H. Kraus, and M. J. Borden, Radiation hardness measurements of new permanent magnet materials for high-intensity linac applications, Technical Report LA-UR-97-3370, Los Alamos, 1997.

[9] K. Halbach, Nucl. Instrum. Meth. **169**, 1 (1980).

[10] D. Barlow, pRad PMQ restoration, LANL Memo, 2008.

[11] C. T. Olinger, Proton radiography of meteorite samples, Technical Report LA-UR-13-26539, Los Alamos, 2013.

[12] D. Barlow, pRad 7x PMQ remagnetization, LANL Memo, 2013.

[13] E. W. Blackmore, Nuclear Science, IEEE Transactions on **32**, 3669 (1985).

[14] J. Cost, R. Brown, A. L. Giorgi, and J. Stanley, Effects of neutron irradiation on nd-fe-b magnetic properties, Technical Report LA-UR-86-4245, Los Alamos, 1986.

[15] R. Brown and J. Cost, Radiation-induced changes in magnetic properties on nd-fe-b permanent magnets, Technical Report LA-UR-87-3043, Los Alamos, 1987.

[16] J. Cost, Sm-co permanent magnets - effects of fast neutron irradiation, Technical Report LA-UR-88-4263, Los Alamos, 1988.

[17] M. Talvitie et al., Journal of Magnetism and Magnetic Materials **102**, 323 (1991).

[18] S. Okuda, K. Ohashi, and N. Kobayashi, Nuclear Instruments and Methods in Physics Research Section B: Beam Interactions with Materials and Atoms **94**, 227 (1994).

[19] C. R. Danly, F. E. Merrill, D. Barlow, and F. G. Mariam, Rev. Sci. Instrum. (2014).

[20] F. Merrill et al., Nucl. Instrum. Meth. B **261**, 382 (2007).

[21] Tridus Magnetics and Assemblies, Demagnetization curves of sintered Nd-Fe-B magnets, http://www.tridus.com/curves.aspx.

[22] D. Nelson, P. J. Barale, M. I. Green, and D. A. VanDyke, The LBNL magnetic-moment sorting system, in *9th International Conference on Magnet Technology*, 1985.

[23] M. Berger, J. Coursey, M. Zucker, and J. Chang, ESTAR, PSTAR, and ASTAR: Computer programs for calculating stopping-power and range tables for electrons, protons, and helium ions (version 1.2.3)., Technical report, NIST, http://physics.nist.gov/Star, 2005.